Learning to reconstruct from saturated data: audio declipping and high-dynamic range imaging

Anonymous authors
Paper under double-blind review

Abstract

Learning based methods are now ubiquitous for solving inverse problems, but their deployment in real-world applications is often hindered by the lack of ground truth references for training. Recent self-supervised learning strategies offer a promising alternative, avoiding the need for ground truth. However, most existing methods are limited to linear inverse problems. This work extends self-supervised learning to the non-linear problem of recovering audio and images from clipped measurements, by assuming that the signal distribution is approximately invariant to changes in amplitude. We provide sufficient conditions for learning to reconstruct from saturated signals alone and a self-supervised loss that can be used to train reconstruction networks. Experiments on both audio and image data show that the proposed approach is almost as effective as fully supervised approaches, despite relying solely on clipped measurements for training.

1 Introduction

Inverse problems appear in various engineering and science applications, such as tomography (Jin et al., 2016), MRI (Lustig et al., 2007) or phase retrieval (Shechtman et al., 2015). They are described by the following forward equation:

$$\boldsymbol{y} = h(\boldsymbol{x}) + \boldsymbol{\epsilon}, \tag{1}$$

where the aim is to recover the ground-truth $\boldsymbol{x} \in \mathcal{X} \subseteq \mathbb{R}^n$ from measurements $\boldsymbol{y} \in \mathcal{Y} \subseteq \mathbb{R}^m$. The set $\mathcal{X}$ defines the support of the of the signal distribution $p(\boldsymbol{x})$, which we refer to as the "signal set". The function $h : \mathbb{R}^n \mapsto \mathbb{R}^m$ represents the forward operator and $\boldsymbol{\epsilon} \in \mathbb{R}^m$ the noise. These problems are often ill-posed due to potential information loss induced by h (for example, if $m < n$) or the existence of an infinite number of solutions. One way of solving this is to impose prior information on $\boldsymbol{x}$, such as piecewise constant assumptions (Rudin et al., 1992). However, choosing the right prior can be challenging and mispecified priors can introduce biases or give poor approximations of the underlying signals. This problem can be mitigated by learning the prior or reconstruction function directly from data. Most learning based methods learn the inverse operator of h on $\mathcal{X}$, $f : \boldsymbol{y} \mapsto \boldsymbol{x}$ from a training dataset containing ground truth with their associated measurements $\{(\boldsymbol{x}_i, \boldsymbol{y}_i)\}_{i=1}^N$ and a neural network $f_{\boldsymbol{\theta}}$ that parameterizes the inverse function. The standard approach computes the parameters $\boldsymbol{\theta} \in \mathbb{R}^p$ by minimizing the mean square error (MSE):

$$\hat{\boldsymbol{\theta}} = \arg\min_{\boldsymbol{\theta}} \sum_{i=1}^{N} \|f_{\boldsymbol{\theta}}(\boldsymbol{y}_i) - \boldsymbol{x}_i\|^2. \tag{2}$$

Despite the good performance in some applications, this approach suffers from two main drawbacks: *(i)* ground-truth images can be particularly difficult or impossible to obtain, e.g., in scientific imaging applications (Belthangady & Royer, 2019), and *(ii)* even when we have access to a ground truth dataset, there might be a significant distribution shift between training and testing.

Self-supervised learning presents an alternative that circumvents some of these limitations (Belthangady & Royer, 2019). This approach operates without the need for ground-truth training data, making it especially

advantageous in scenarios where obtaining such datasets is expensive or impractical. Furthermore, self-supervised learning can be trained on measurement data directly, thus mitigating the challenge of distribution shift.

Learning from measurement data only is particularly challenging when the forward operator is not invertible (Tachella et al., 2023). If the forward operator is linear, self-supervised learning is possible by assuming that the underlying set of clean signals is invariant to a set of transformations, such as rotations or translations (Chen et al., 2021). This also holds for the non-linear problem of reconstructing heavily quantized signals (1-bit measurements) (Tachella & Jacques, 2023). Here we show that invariance to rotations or translations is not enough for learning from clipped measurement data alone, and instead prove that invariance to amplitude is sufficient for fully self-supervised learning. We propose a self-supervised loss that enforces equivariance to changes in amplitude, and show throughout a series of experiments that our method can achieve performance comparable to fully supervised methods. A preliminary version of this work was presented in anonymous author (2024), and here we generalize to a larger class of signals such as images, and propose a theoretical framework showing sufficient conditions for learning to recover signals from saturated measurements alone. In summary, the contributions of this work are threefold:

- We provide necessary conditions for signal recovery under a known signal set, and also demonstrate, under an invariance assumption, that the signal set can be identified with a sufficient number of observed measurements;
- We propose a self-supervised loss that can be used to train neural networks for audio declipping and High-Dynamic Range (HDR) imaging;
- We show that this method can achieve comparable performance to fully supervised methods on both audio and image data.

The rest of the paper is structured as follows: Section 2 reviews related work concerning self-supervised learning and state-of-the-art declipping methods. Section 3 introduces our theoretical framework, focusing on model identification—i.e., determining underlying signal set from observations—and signal recovery. From there, in Section 4 we describe how one can practically define and minimize a self-supervised cost function with scale invariance. Section 5 presents experimental results that validate our approach.

2 Related work

2.1 Self-supervised learning for inverse problems

Self-supervised methods allow to train reconstruction networks using only measurement data (Chen et al., 2021). Existing methods can be separated into two categories: the ones that handle the noise of the problem, e.g., Noise2X methods (Lehtinen et al., 2018; Krull et al., 2019), and the others that handle non-invertible forward operators (Tachella et al., 2023). The last set of methods mostly focuses on the case a linear operator where the loss of information is associated to its nullspace. It is possible to overcome this missing information by *(i)* accessing measurements from several operators with different nullspaces (Daras et al., 2023; Tachella et al., 2023), or *(ii)* by assuming that the signal distribution is invariant to a set of transformations such as translations or rotations, a method known as equivariant imaging (EI) (Chen et al., 2021). The EI framework is well studied for linear inverse problems, both in terms of applications (Scanvic et al., 2024; Chen et al., 2021) and theory (Tachella et al., 2023). To the best of our knowledge, the only case of nonlinear inverse problems analyzed using the invariance approach is one-bit compressed sensing (Tachella & Jacques, 2023).

2.2 Audio declipping

Several unsupervised techniques for audio declipping have been proposed (Zaviska et al., 2021; Kitic et al., 2013; Gaultier et al., 2021), many of which make use of variational methods with priors such as sparsity in certain bases (e.g. Fourier domain). Both ℓ_0 and ℓ_1-minimization approaches are commonly employed, often

solved using dedicated optimization algorithms, with social sparsity as one of the best performing (Siedenburg et al., 2014). Learning-based techniques, such as dictionary learning, have also shown to be effective, where a dictionary is trained from time windows of the clipped signal to represent it as a sparse vector. Additionally, methods incorporating prior knowledge based on human perception (Defraene et al., 2013), or using multichannel data (Ozerov et al., 2016; Gaultier et al., 2018), have been used to improve performance. Diffusion models trained on a supervised way (i.e., with ground-truth references) have also been studied in the context of declipping. (Moliner et al., 2023).

2.3 High Dynamic Range images

The dynamic range in images refers to the difference between the brightest and darkest values. Since camera sensors and displays have limitations in capturing and showing both dark and bright regions, this often results in lost details in these zones. To address this, various techniques are employed to extend the dynamic range of images. One common method is exposure bracketing (Mertens et al., 2007), which combines multiple photos at different exposures for higher quality but requires long exposures and a stationary target to avoid misalignment. Another approach is modulo sensing (Contreras et al.), a promising technique, though it is still limited by the unavailability of commercial hardware. Finally, supervised deep learning methods, such as the ones proposed by Eilertsen et al. (2017), utilize a single image to estimate a high dynamic range. However, these methods require a large dataset of ground truths to train the model effectively, which can be a significant limitation.

2.4 Signal recovery guarantees for saturated measurements

Some theoretical works have analysed the feasibility of the signal recovery problem from saturated observations. Following a compressive sensing approach (Candes & Wakin, 2008), Foucart & Needham (2016) present unique recovery guarantees for the case Gaussian measurements and an ℓ_1 minimization approach, showing that sparse vectors with low magnitude can be uniquely recovered with high probability.

3 Analysis for model identification and signal recovery

3.1 Problem formulation

We consider the forward formulation $\boldsymbol{y} = \eta(\boldsymbol{x})$, where $\eta : \mathbb{R} \to \mathbb{R}$ is the element-wise clipping operator with threshold levels μ_1, μ_2:

$$\eta(u) = \begin{cases} \mu_1 & \text{if} \quad u \leq \mu_1, \\ u & \text{if} \quad u \in (\mu_1, \mu_2), \\ \mu_2 & \text{if} \quad u \geq \mu_2. \end{cases}$$

For our examples with audio and synthetic signals, we use a symmetric threshold $\mu_1 = -\mu_2 = \mu$. For images, we only consider an upper threshold, where $\mu_1 = 0$ and $\mu_2 = 1$, assuming positive signals $\boldsymbol{x}$, as camera sensors do not suffer saturation from below. Indeed, under low-light conditions, the sensor produces a weaker signal, which may lead to noise or reduced image quality, but not to saturation. We assume that μ_1 and μ_2 are known and that we have a dataset of saturated signals $\{\boldsymbol{y}_i\}_{i=1}^N$. We aim to learn the reconstruction function $f_{\boldsymbol{\theta}}$ using the measurement dataset alone. We will therefore consider the following two theoretical questions: *(i) model identification*: can we uniquely identify the signal set given the set of observations $\{\boldsymbol{y}_i\}_{i=1}^N$? In other words, we want to know if it is possible to find the support of the signal distribution $\mathcal{X}$ from measurement data alone as $N \to \infty$, and some mild priors on $\mathcal{X}$ (e.g. invariance to transformations). If the set $\mathcal{X}$ can be identified, we could then hope to recover the signal $\boldsymbol{x}$ from a single observation $\boldsymbol{y}$ via the following program:

$$\hat{\boldsymbol{x}} \in \arg\min_{\boldsymbol{x} \in \mathcal{X}} \|h(\boldsymbol{x}) - \boldsymbol{y}\|^2. \tag{3}$$

(ii) Signal recovery: is there a unique solution to the problem in Equation (3)? In other words, can we uniquely recover the signal $\boldsymbol{x}$ from observations $\boldsymbol{y}$ knowing the set $\mathcal{X}$? There may be a unique solution for one, both, or neither of the problems (Tachella et al., 2023). Blind compressed sensing is an example

where we can have signal recovery if the dictionary is known, but we cannot identify the dictionary from measurement data alone (Gleichman & Eldar, 2011). On the contrary, we can identify the signal set from rank-one measurements without being able to recover the signals associated with each measurement. (Chen et al., 2015). In the following, we will use "identify" only for finding the set $\mathcal{X}$ given a measurement set $\mathcal{Y}$, and "recovery" for finding a vector $\boldsymbol{x}$ given a measurement $\boldsymbol{y}$.

3.2 Model identification.

In this section, we will focus on the case where the full set of measurements $\mathcal{Y}$ is observed, although in practice we only observe $\{\boldsymbol{y}_i\}_{i=1}^N$. We thus study the conditions for identifying $\mathcal{X}$ from the set of saturated signals $\mathcal{Y} = \eta(\mathcal{X})$.

It may be interesting to note that in some situations we can easily identify the signal set. This happens in the trivial case where the whole signal set is below the saturation threshold.

Example 1. *In the symmetric case with threshold level μ, if $\|\boldsymbol{y}\|_\infty < \mu$ for all $\boldsymbol{y} \in \mathcal{Y}$, then $\mathcal{X} = \mathcal{Y}$.*

Proposition 1. *Without any assumption on $\mathcal{X}$ and the presence of saturated signals, we cannot guarantee model identification. See Remark 1, which can be used as proof of this statement.*

We thus need to consider some assumptions on $\mathcal{X}$ to identify the signal set from $\mathcal{Y}$. As done in equivariant imaging (Chen et al., 2021), we can consider the group of transformations G for which the signal set is invariant. The reason is that the invariance to transformations $\{\boldsymbol{T}_g\}_{g\in G}$ gives us access to the sets $\mathcal{Y}_g = \eta(\boldsymbol{T}_g\mathcal{X})$ for all $g \in G$. Indeed, we can see $\mathcal{Y}$ as a set of measurements associated with the set $\mathcal{X}$ for different forward operators $\eta(\boldsymbol{T}_g\cdot)$, as we have that:

$$\mathcal{Y}_g = \eta(\boldsymbol{T}_g\mathcal{X}) = \eta(\mathcal{X}) = \mathcal{Y} \quad \text{if} \quad \boldsymbol{T}_g\mathcal{X} = \mathcal{X}.$$

We then need to identify which groups of transformations can help in identifying $\mathcal{X}$. We cannot use the classical groups considered in the linear framework (shift or rotation) as these transformations commute with the operator η. As shown in the following proposition, if the transformations commute with η, they do not help to identify the signal set.

Proposition 2. *Let G be a group, if we cannot identify $\mathcal{X}$ from $\mathcal{Y} = \eta(\mathcal{X})$ and if for all $g \in G$, the transformations $\boldsymbol{T}_g$ commute with $\eta(\cdot)$, then we cannot identify $\mathcal{X}$ from $\mathcal{Y}_g = \eta(\boldsymbol{T}_g\mathcal{X})$ for all $g \in G$.*

Proof. Let G such that for all $g \in G$, $\boldsymbol{T}_g\eta(\cdot) = \eta(\boldsymbol{T}_g\cdot)$. We have access to all measurements associated with the different transformations of the signals:

$$\bigcup_{g\in G} \mathcal{Y}_g = \{y_g = \eta(T_g\boldsymbol{x}) : \forall g \in G,\ \forall \boldsymbol{x} \in \mathcal{X}\}.$$

As $\boldsymbol{T}_g$ and η commute, we have

$$\bigcup_{g\in G} \mathcal{Y}_g = \{y_g = \boldsymbol{T}_g\eta(\boldsymbol{x}) : \forall g \in G,\ \forall \boldsymbol{x} \in \mathcal{X}\} = \bigcup_{g\in G} \boldsymbol{T}_g\eta(\mathcal{X}),$$

and so we cannot identify $\mathcal{X}$ from that set since it doesn't bring us more information than $\eta(\mathcal{X})$; the set of measurements is a function of $\eta(\mathcal{X})$. □

Example 1 shows us that the norm of $\boldsymbol{x}$ has an impact on the feasibility of reconstructing the signal, which gets us to consider the group action of scaling.

Definition 1 (Scale invariance)**.** *We say that $\mathcal{X}$ is scale invariant if*

$$g\mathcal{X} = \mathcal{X} \text{ for all } g \in \mathbb{R}_+^*. \tag{4}$$

A set that is scale-invariant is called a cone (Boyd & Vandenberghe, 2004).

Proposition 3. *For any two distinct conic sets $\mathcal{X} \neq \mathcal{X}'$, we have that $\eta(\mathcal{X}) \neq \eta(\mathcal{X}')$.*

Proof. Let the open set $\mathbb{B}_\mu = \{\boldsymbol{u} \in \mathbb{R}^n \ : \ \|\boldsymbol{u}\|_\infty < \mu\}$ with radius $\mu > 0$. We recall that we note $\mathcal{Y}$ the set of measurement $\mathcal{Y} = \eta(\mathcal{X})$. Taking the set of unsaturated signals in $\mathcal{X}$, that is $\mathcal{X} \cap \mathbb{B}_\mu$, the operator η has no impact on them and therefore

$$\mathcal{X} \cap \mathbb{B}_\mu = \eta(\mathcal{X} \cap \mathbb{B}_\mu).$$

Moreover, if $\boldsymbol{x}$ is in $\mathbb{B}_\mu$, then $|\eta(\boldsymbol{x})| < \mu$, therefore

$$\eta(\mathcal{X} \cap \mathbb{B}_\mu) \subset \mathcal{Y} \cap \mathbb{B}_\mu.$$

But if $\boldsymbol{y}$ is in $\eta(\mathcal{X}) \cap \mathbb{B}_\mu$, then $\boldsymbol{y}$ never reaches the threshold μ or $-\mu$, and there is thus an $\boldsymbol{x}$ in $\mathcal{X} \cap \mathbb{B}_\mu$ such that $\boldsymbol{y} = \eta(\boldsymbol{x}) = \boldsymbol{x}$, i.e.,

$$(\eta(\mathcal{X}) \cap \mathbb{B}_\mu) \subset (\mathcal{X} \cap \mathbb{B}_\mu)$$

showing finally that

$$\mathcal{Y} \cap \mathbb{B}_\mu = \mathcal{X} \cap \mathbb{B}_\mu.$$

Defining $\hat{\mathcal{X}} = \left\{g\boldsymbol{y} \ : \ g \in \mathbb{R}_+^*, \ \boldsymbol{y} \in \mathcal{Y} \cap \mathbb{B}_\mu\right\}$ as the conic extension of $\mathcal{Y} \cap \mathbb{B}_\mu$. We will show that $\hat{\mathcal{X}} = \mathcal{X}$.

Inclusion $\mathcal{X} \subset \hat{\mathcal{X}}$: Let $\boldsymbol{x} \in \mathcal{X}$. Then, there exists $c > 0$ such that $\boldsymbol{y} = c\boldsymbol{x}$ belongs to $\mathcal{X} \cap \mathbb{B}_\mu$. Therefore, $\boldsymbol{x} = \frac{1}{c}\boldsymbol{y}$ belongs to $\hat{\mathcal{X}}$, which implies $\mathcal{X} \subset \hat{\mathcal{X}}$.

Inclusion $\hat{\mathcal{X}} \subset \mathcal{X}$: Let $\hat{\boldsymbol{x}} \in \hat{\mathcal{X}}$. By definition, there exist $g \in \mathbb{R}_+^*$ and $\boldsymbol{y} \in \mathcal{Y} \cap \mathbb{B}_\mu$ such that $\hat{\boldsymbol{x}} = g\boldsymbol{y}$. Since $\mathcal{Y} \cap \mathbb{B}_\mu = \mathcal{X} \cap \mathbb{B}_\mu$, we have $\boldsymbol{y} \in \mathcal{X}$. As $\mathcal{X}$ is a cone, it follows that $\hat{\boldsymbol{x}} = g\boldsymbol{y} \in \mathcal{X}$. Thus, we conclude that $\hat{\mathcal{X}} \subset \mathcal{X}$, completing the proof.

□

Remark 1. *For asymmetric clipping, the same result can be obtained for $\mu_1 \leq 0 < \mu_2$ and $\mathcal{X} \subset \mathbb{R}_+^n$. However, we can find a 2-dimensional counter example for $0 < \mu_1 < \mu_2$: we choose $\mathcal{X}_1 = \{a\boldsymbol{x}_1 \ : \ a \in \mathbb{R}^+\}$ and $\mathcal{X}_2 = \{a\boldsymbol{x}_2 \ : \ a \in \mathbb{R}^+\}$ with $\boldsymbol{x}_1 = (\mu_2, \frac{\mu_1}{2})^\top$ and $\boldsymbol{x}_2 = (\mu_2, \frac{\mu_1}{3})^\top$. Then $\mathcal{X}_1$ and $\mathcal{X}_2$ have the same measurement set:*

$$\mathcal{Y} = \{(t, \mu_1) : t \in (\mu_1, \mu_2)\} \cup \{(\mu_2, t) : t \in (mu_1, \mu_2)\}.$$

3.3 Signal recovery

Sufficient conditions for signal recovery generally depend on the dimension of $\mathcal{X}$ (Sauer et al., 1991). Following previous work in compressed sensing (Sauer et al., 1991; Falconer, 2013), we use the box-counting dimension, a measure of the complexity of a set which generalizes several notions of dimension.

Definition 2. *The upper box-counting dimension of a compact subset $\mathcal{X}$ is*

$$\dim(\mathcal{X}) = \limsup_{\epsilon \to 0} \frac{\log\left[N_{\mathcal{X}}(\epsilon)\right]}{-\log(\epsilon)},$$

where $N_{\mathcal{X}}(\epsilon)$ is the covering number, i.e., the minimum number of closed balls of radius ϵ (with respect to the norm $\|\cdot\|_2$) with centres in $\mathcal{X}$ needed to cover $\mathcal{X}$.

It can be applied to various structures:

- Vector spaces: The box-counting dimension of a space $\mathbb{R}^k$ intersected with the unit ball is k, corresponding to the classical geometrical dimension.
- Manifolds: For a manifold of dimension k, the box-counting dimension is k, consistent with its geometric dimension.
- Bounded k-sparse sets: In high dimensional spaces, the box-counting dimension reflects the effective dimension k rather than the ambient dimension n.

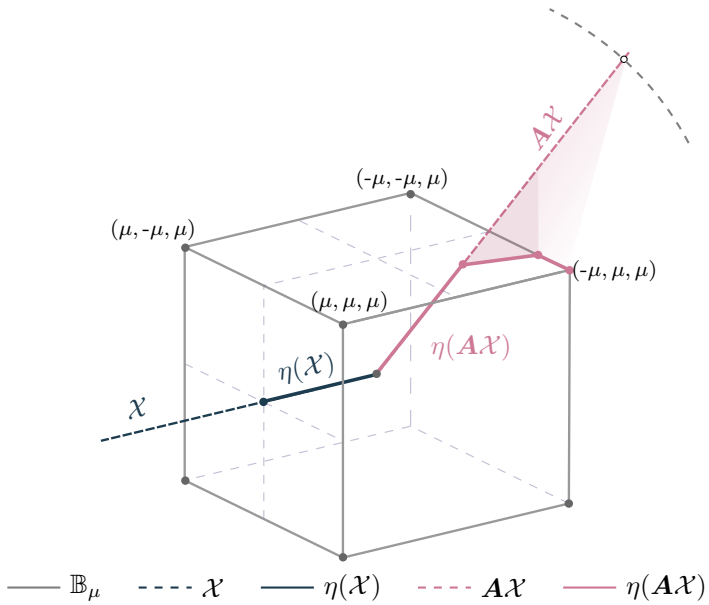

Figure 1: Example in 3 dimensions illustrating Theorem 1. The black set presents a particularly challenging scenario in which all saturated signals are projected to the same point. In contrast, with high probability on $\boldsymbol{A}$, the colored set enables recovery of more signals with moderate norms, as points in $\mathcal{X}$ beyond a certain radius— which is connected to the signal norm when $\boldsymbol{A}$ is Gaussian—are all projected onto a single corner, showing the non-injectivity beyond this radius.

Thus, the box-counting dimension uniquely determines the dimension of these various objects, providing a flexible framework for measuring the dimension of objects that can appear in compressive sensing or inverse problems.

We approach the problem of signal recovery by considering, for a conic signal set $\mathcal{X}$, its normalized version:

$$S_{\mathcal{X}} = \left\{ \frac{\boldsymbol{x}}{\|\boldsymbol{x}\|_2} \ : \ \boldsymbol{x} \in \mathcal{X} \right\}$$

and the open bounded set

$$\mathcal{X}_R = \{\boldsymbol{x} \in \mathcal{X} \ : \ \|\boldsymbol{x}\|_2 < R\}.$$

When studying the signal recovery problem, one observes that pathological cases where $\eta(\boldsymbol{x}_1) = \eta(\boldsymbol{x}_2)$ for $\boldsymbol{x}_1 \neq \boldsymbol{x}_2$ may arise even when $\dim(\mathcal{X})$ is small, as illustrated in Figure 1. As the operator η acts as a projection onto the cube $\mathbb{B}_\mu$ if the signal set is orthogonal to one of the cube's faces, it becomes impossible to recover a signal once it reaches that face. However, we expect such cases to be relatively rare, and therefore we study the problem by randomizing the orientation. To this end, as it is common signal recovery analyses (Ahmed et al., 2013), we consider the operator $\eta(\boldsymbol{A}\cdot)$, where $\boldsymbol{A} \in \mathbb{R}^{m\times n}$ is a random Gaussian matrix, which acts as a random rotation of the signal set. An illustration is provided in Figure 1. The following theorem provides sufficient conditions on the number of measurements and the maximum radius R to ensure, with high probability, that distances between points in the set $\mathcal{X}_R$ are approximately preserved after applying $\eta(\boldsymbol{A}\cdot)$. Section 5.2.1 provides a simplified example demonstrating how this matrix effectively addresses degenerate cases.

Theorem 1. *If the set $S_{\mathcal{X}}$ has a finite upper box-counting dimension $\dim(S_{\mathcal{X}}) < k$ and $\boldsymbol{A} \in \mathbb{R}^{m\times n}$ is such that $A_{ij} \sim \mathcal{N}\left(0, \frac{1}{m}\right)$, then there is an absolute constant $C > 0$ and a signal set dependent constant $\epsilon^* \in (0, 1/2)$ such that, if $m \geq k \log\left(\frac{1}{\epsilon^*}\right)$, we have for a radius $R < \sqrt{m}\mu\left(\frac{1}{2} - \frac{k+1}{m}\right)$:*

$$\mathbb{P}\left(\eta(\boldsymbol{A}\boldsymbol{x}) = \eta(\boldsymbol{A}\boldsymbol{u}) \text{ for some } \boldsymbol{x} \neq \boldsymbol{u} \in \mathcal{X}_R\right) \leq 12e^{-Cm}. \tag{5}$$

In other words, we measure the probability that the mapping $\eta \circ \boldsymbol{A}$ is not injective (and therefore impossible to invert) over $\mathcal{X}_R$.

To consider the initial problem, that is, the forward operator $\eta(\cdot)$, we may introduce an assumption on $\mathcal{X}$ by considering it as a cone of the form

$$\mathcal{X} = \{\boldsymbol{A}z : z \in \mathcal{Z}\},$$

here $\mathcal{Z}$ is a cone with $S_{\mathcal{Z}}$ of box-dimension k and $\boldsymbol{A} \in \mathbb{R}^{n\times n}$ is such that $A_{ij} \sim \mathcal{N}\left(0, \frac{1}{n}\right)$. We can apply Theorem 1 in the case of a random rotation $m = n$, to show that a signal $\boldsymbol{x}$ can be recovered with high probability if $\|\boldsymbol{x}\|_2 < \|\boldsymbol{A}\|R$, where $\|\boldsymbol{A}\|$ denotes the norm of the operator $\boldsymbol{A}$, and in the case of Gaussian square matrix of variance $\frac{1}{n}$, it is close to 2 (Vershynin, 2018).

The proof of the theorem is provided in the Appendix A, and sketched in Figure 1. It consists in showing that the same measurement vector cannot be associated with two distinct signals, with high probability. The core idea of the proof is to decompose the probability that the mapping is not injective into two parts: Given two distinct signals, we control, the probability that the number of common unsaturated measurements is small (thus making it impossible to differentiate between 2 signals). On the other hand, we control the probability that two signals have the same common unsaturated measurements given that the number of saturated measurements is low and so it is acceptable to ignore them.

Let us stress that in Theorem 1 we cannot set an upper bound on the probability in Equation (5) for all signals in $\mathcal{X}$ and need to limit this space to bounded signals from $\mathcal{X}_R$. Some signals in $\mathcal{X}$ with an excessive norm cannot be recovered as they have too numerous saturated measurements. In Figure 1, this is illustrated by the accumulation, after saturation, of signals in the corners of the cube, particularly when signals have high norms, i.e., far from the cube's center. When all measurements are saturated, or equivalently when μ tends to 0, we expect to recover the behavior of 1-bit compressive sensing (Tachella & Jacques, 2023), where $\boldsymbol{x}$ can only be estimated up to a non-zero error. This is why we focus on signals with low norms. Theorem 1 can be seen as a generalization of Foucart & Needham (2016, Theorem 1), to more general low-dimensional sets, going beyond sets of k-sparse signals.

4 Self-supervised learning approach

Given the positive theoretical results regarding model identification and signal recovery of the previous section, we now propose a method for learning from saturated signals $\{\boldsymbol{y}_i = \eta(\boldsymbol{x}_i)\}_{i=1}^N$. We first introduce the loss functions used to train the network, then describe the network architecture and implementation details used for the reconstruction.

4.1 Loss functions

Measurement consistency (MC) loss: in the absence of noise, a good reconstruction method should provide an estimate that is consistent with the observations, i.e., for all measurements $\boldsymbol{y}$, we should have

$$\eta(f_{\boldsymbol{\theta}}(\boldsymbol{y})) = \boldsymbol{y}.$$

Measurement consistency means that the reconstructed signal produces the same measurements as those that were originally observed. Ensuring MC is crucial, as it guarantees that estimates adhere to observations. However, it does not necessarily mean that the solution is unique since multiple solutions could be consistent with the same measurements. A straightforward loss function for imposing measurement consistency is

$$\mathcal{L}_{\text{NMC}}(\boldsymbol{\theta}) = \sum_{i=1}^{N} \|\boldsymbol{y}_i - \eta\left(f_{\boldsymbol{\theta}}(\boldsymbol{y}_i)\right)\|^2, \tag{6}$$

which we will call the naive measurement consistency loss. If at the first training steps, the network predicts a value $\hat{x}_j$ above the threshold, the gradient will be zero due to the η operator and thus get stuck on this prediction, preventing the network from learning. This is particularly problematic if y_j is below the

threshold, since we know that the true value is $x_j = y_j$. We therefore choose to use the MSE where the signal is not saturated according to the following loss:

$$\mathcal{L}_{\text{MC}}(\boldsymbol{\theta}) = \sum_{i=1}^{N} \|\rho(f_{\boldsymbol{\theta}}(\boldsymbol{y}_i), \boldsymbol{y}_i)\|^2 \tag{7}$$

where ρ is applied element-wise as:

$$\rho(a, b) = \mathbb{1}_{\{|b|<\mu\}}|b - a| + \mathbb{1}_{\{b=\mu\}}(b - a)_+ + \mathbb{1}_{\{b=-\mu\}}(a - b)_+,$$

where $\mathbb{1}(\cdot)$ the indicator function and $(\cdot)_+$ the positive function. See Figure 2 for a comparison of these functions.

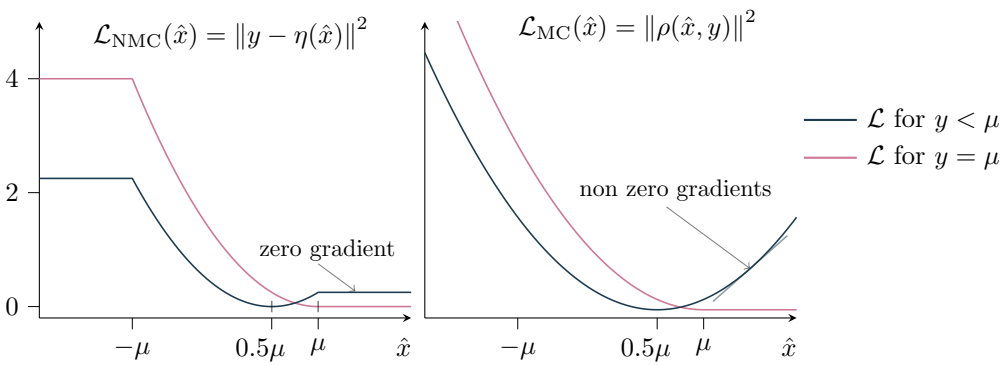

Figure 2: $\mathcal{L}_{\text{NMC}}$ compared to $\mathcal{L}_{\text{MC}}$. On the left: Curve of the $\mathcal{L}_{\text{NMC}}$ in one dimension for two examples in both cases saturated and not. On the right: Curve of the new $\mathcal{L}_{\text{MC}}$ for the same two examples.

However, even with this new loss, we cannot hope to learn the correct reconstruction function. Minimizing $\mathcal{L}_{\text{MC}}$ allows us to learn a measurement consistent solution $f_{\boldsymbol{\theta}}$, but this solution could be of the form:

$$f_{\boldsymbol{\theta}}(\boldsymbol{y})_j = \begin{cases} y_j & \text{if} \quad |y_j| \leq \mu \\ v(y_j) & \text{if} \quad |y_j| = \mu \end{cases} \tag{8}$$

with v being *any* function lying beyond the threshold level μ i.e., $v(y_j)$ belongs to the preimage $\eta^{-1}(\{-\mu, \mu\})$. For example, the function $f_{\boldsymbol{\theta}}(\boldsymbol{y}) = \boldsymbol{y}$ is a minimizer of Equation (7).

Equivariance loss: To effectively learn in the saturated region, we use the amplitude invariance assumption of the signal set defined above, going beyond the limitations imposed by measurement consistency alone.

To enforce this invariance property on the reconstruction network, we note that since $g\boldsymbol{x} \in \mathcal{X}$, the function $f_{\boldsymbol{\theta}}$ must be capable of reconstructing both $\boldsymbol{x}$ and $g\boldsymbol{x}$ for all $\boldsymbol{x}$ in $\mathcal{X}$ and $g \in \mathbb{R}_+$, that is:

$$f_{\boldsymbol{\theta}}\left(\eta(g\boldsymbol{x})\right) = g\boldsymbol{x} \quad \text{and} \quad f_{\boldsymbol{\theta}}(\eta(\boldsymbol{x})) = \boldsymbol{x}. \tag{9}$$

Thus, we can conclude that:

$$f_{\boldsymbol{\theta}}\big(\eta(g\boldsymbol{x})\big) = g f_{\boldsymbol{\theta}}\big(\eta(\boldsymbol{x})\big) \text{ for all } \boldsymbol{x} \in \mathcal{X}, \text{ and } g \in \mathbb{R}_+. \tag{10}$$

Hence, the composition of $f_{\boldsymbol{\theta}}$ with η should be equivariant with respect to the multiplicative group $(\mathbb{R}_+, \cdot)$. To ensure this, we propose a loss function that enforces this equivariance property:

$$\mathcal{L}_{\text{EI}}(\boldsymbol{\theta}) = \sum_{i=1}^{N} \mathbb{E}_{g \sim p_g} \left[\left\| g f_{\boldsymbol{\theta}}\left(\boldsymbol{y}_i\right) - f_{\boldsymbol{\theta}}\big(\eta\left(g f_{\boldsymbol{\theta}}\left(\boldsymbol{y}_i\right)\right)\big) \right\|^2 \right]. \tag{11}$$

We can observe a connection with Proposition 3: for $N \to \infty$, after rescaling, the sum becomes an expectation over a distribution supported on $\mathcal{Y}$, and the expectation over g basically acts as a (restricted) conic extension of that support.

The expectation is evaluated with respect to a specific distribution p_g over the multiplicative group, which, in principle, could be any unbounded distribution over $\mathbb{R}_+$. However, in practical scenarios, signals are typically limited in amplitude, making it sufficient to use a distribution defined over a finite range $[g_{\min}, g_{\max}]$ (not necessarily uniform). The parameters $(g_{\min}, g_{\max})$ were determined empirically: setting $g_{\max}$ too low prevents the network from learning effectively, while excessively large values cause instability.

We could also extend Equation (11) to include transformations not limited to scale invariance, such as affine group transformations of the form $\boldsymbol{x} \to a\boldsymbol{x} + b\mathbf{1}$, where $(a, b) \in \mathbb{R}_+ \times \mathbb{R}$ and $\mathbf{1} = (1, \ldots, 1)^\top \in \mathbb{R}^n$.

The final loss function is a combination of the measurement consistency and equivariance losses:

$$\mathcal{L}(\boldsymbol{\theta}) = \mathcal{L}_{\mathrm{MC}}(\boldsymbol{\theta}) + \lambda \mathcal{L}_{\mathrm{EI}}(\boldsymbol{\theta}). \tag{12}$$

The parameter λ is a positive hyperparameter that controls the trade-off between the two losses.

4.2 Network architecture

4.2.1 Core architecture

The proposed self-supervised loss can be used with any network architecture $f_{\boldsymbol{\theta}}$. For most of the experiments reported here, we choose the well-known U-Net neural network for the reconstruction function $f_{\boldsymbol{\theta}}$ (Ronneberger et al., 2015), which is well-suited for capturing the relevant (temporal or spatial) correlations in natural signals. The details of the architecture vary depending on the type of data, audio or image, and are explained in the experiment section.

4.2.2 Bias-free neural network

We choose a bias-free version of the U-Net, to preserve the scale invariance assumption (Mohan et al., 2020). This is because a feedforward neural network with ReLU activation functions and without bias defines a homogeneous function:

$$f_{\boldsymbol{\theta}}(g\boldsymbol{y}) = g f_{\boldsymbol{\theta}}(\boldsymbol{y}) \quad \forall g \in \mathbb{R}_+.$$

This gives $f_{\boldsymbol{\theta}}(g\boldsymbol{y}) \underset{g \to 0}{\longrightarrow} 0$, which is particularly necessary for unsaturated signals. Figure 3 shows an example where a biased network cannot reconstruct an unsaturated signal.

4.3 Masking

A key aspect of the threshold operator is that, by knowing the threshold levels, we can identify the unsaturated, and therefore non-degraded, portion of the signal. While the measurement consistency loss encourages the network to preserve the unsaturated part, it does not guarantee strict adherence to this constraint. To address this limitation, we can enforce measurement consistency more rigorously by employing the following masking method, comparable to a more structured skip connection architecture. The estimated signals $\hat{\boldsymbol{x}}$ are computed using an element-wise linear blending between the outputs of the network $f_{\boldsymbol{\theta}}(\boldsymbol{y})$ and the measurements, that is

$$\hat{x}_j = (1 - b_j) y_j + b_j f_{\boldsymbol{\theta}}(\boldsymbol{y})_j. \tag{13}$$

By choosing an appropriate blend value b_j for all sample points or pixels, the blend works as a mask that modifies only saturated measurements, avoiding artifacts in the unsaturated parts.

$$b_j = \begin{cases} 0 & \text{if } |y_j| < \mu \\ 1 & \text{if } |y_j| = \mu \end{cases}$$

An example of an image and its associated mask is shown in Figure 4.

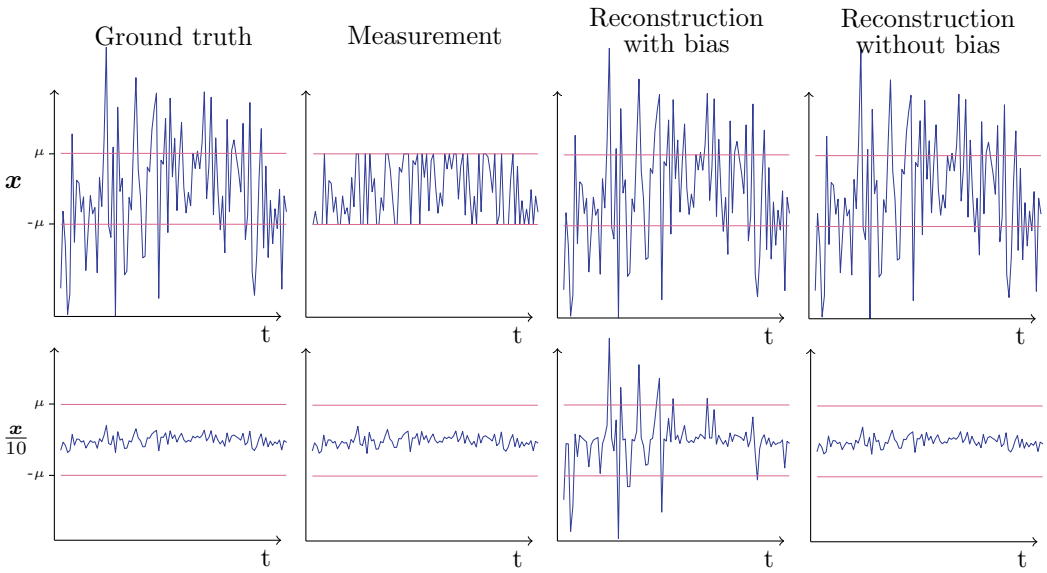

Figure 3: An example where the reconstruction is learned through the bias (third column) which prevents the reconstruction for low amplitude measurements. On the first row, we consider a signal $\boldsymbol{x}$, on the second row $\frac{\boldsymbol{x}}{10}$.

$\boldsymbol{y}$ The blending mask $\boldsymbol{b}$

Figure 4: An image with its associated blending mask. The mask is white where a channel is saturated and black when none is saturated.

5 Experiments

We begin by presenting experiments on toy datasets, where we can control the properties of the signal set. The first experiment uses a dataset associated to a one-dimensional vector space that is invariant to amplitude. The second experiment is performed using various datasets generated by sampling vectors from random k-dimensional subspaces. To generate these datasets, we first control the dimension of the vector space, followed by the saturation proportion for each sampled vector. The reconstruction is then evaluated based on these varying parameters. Next, we conduct experiments on real-world music data, and we compare our method to several state-of-the-art techniques. Finally, we conclude with experiments on two-dimensional signals, where we aim to reconstruct HDR images.

5.1 Metrics

Two common metrics for evaluating the quality of reconstructions are the Signal-to-Distortion Ratio (SDR) and Peak Signal-to-Noise Ratio (PSNR). PSNR is more suitable for image quality assessment, as it incorpo-

rates a maximum possible pixel value, allowing for a clearer comparison of signal fidelity. SDR, on the other hand, is generally applied to audio signals because it does not require knowledge of the maximum possible value. Although we do not know this value for HDR images, we still use PSNR to provide a more relevant comparison with other works. The PSNR and SDR metrics are defined as follows:

$$\mathrm{PSNR}(\boldsymbol{x}, \hat{\boldsymbol{x}}) = 20 \log_{10} \left(\frac{1}{\|\boldsymbol{x} - \hat{\boldsymbol{x}}\|_2} \right), \tag{14}$$

$$\mathrm{SDR}(\boldsymbol{x}, \hat{\boldsymbol{x}}) = 20 \log_{10} \left(\frac{\|\boldsymbol{x}\|_2}{\|\boldsymbol{x} - \hat{\boldsymbol{x}}\|_2} \right). \tag{15}$$

Both metrics are referred to as distortion metrics since they assess the fidelity of the reconstruction process. In addition to distortion metrics, perception metrics could be used to evaluate the quality of the reconstruction, offering a more accurate measure of how changes to a signal or image affect human perception. In this work, we employ the widely adopted metric Perceptual Evaluation of Speech Quality (PESQ) to evaluate audio signals. For image, we use the Natural Image Quality Evaluator (NIQE), a no-reference (no ground-truth needed) metric that estimates image quality. While perceptual metrics are particularly relevant for applications like music audio, where subjective experience plays a key role, they are less suitable for signals where preserving critical information is essential, as they tend to permit greater hallucination - introducing elements that were not part of the original signal, potentially compromising the accuracy of the reconstruction. Blau & Michaeli (2018) study the impossibility of algorithms to optimize both perception and distortion metrics, known as the perception-distortion tradeoff.

5.2 Toy datasets

5.2.1 MNIST experiment

In this example, we use a toy signal set, generated from a single signal and augmented with its scaled versions, i.e. $\mathcal{X} = \{e\boldsymbol{x}_0 : e \in \mathbb{R}_+^*\}$ for $\boldsymbol{x}_0$ fixed. In practice, we take an image $\boldsymbol{x}$ from MNIST and create the dataset $\mathcal{D} = \{e_i \boldsymbol{x}_0\}_{i=1}^N$ with e_i a realization of a random variable with exponential distribution of mean 2, for $i \in \{1, \ldots, N\}$. This dataset has two interesting properties: it is scale invariant, and we cannot have unique signal recovery as shown in Figure 5.

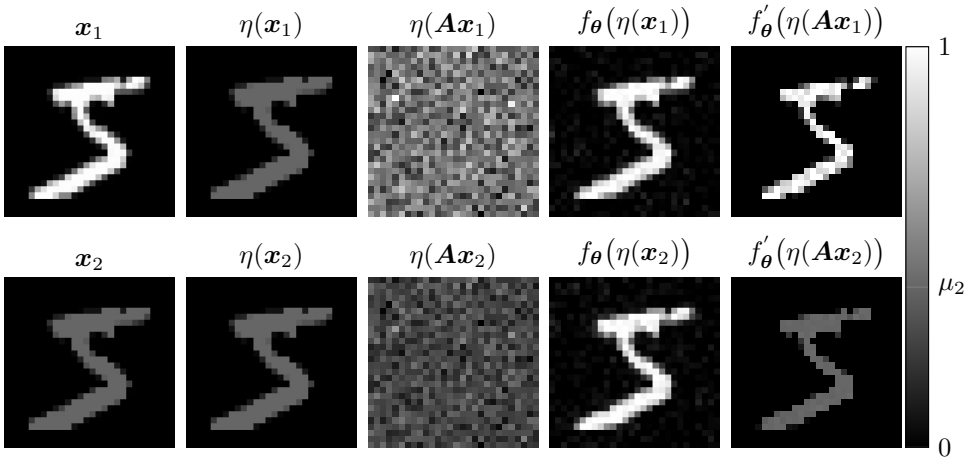

Figure 5: Example where two different signals $\boldsymbol{x}_1, \boldsymbol{x}_2$ have the same measurement $\eta(\boldsymbol{x}_1), \eta(\boldsymbol{x}_2)$ and so the network $f_{\boldsymbol{\theta}}$ fails to recover them both (the second and fourth columns). Adding randomness implies that the two measurements are not equal anymore, and so a network $f'_{\boldsymbol{\theta}}$ can reconstruct the original signal (the third and fifth columns).

Measurements are obtained by applying the forward function $\eta(\boldsymbol{A}\cdot)$ with $\boldsymbol{A}$ an orthogonal matrix and threshold levels $\mu_1 = 0,\ \mu_2 = 0.4$. The matrix $\boldsymbol{A}$ is drawn randomly with respect to the Haar measure (Mezzadri,

2007). While Figure 5 shows that it is impossible without $\boldsymbol{A}$ to recover the original signals, adding randomness in the forward operator solves this issue, as illustrated in Figure 1. Figure 6 shows that the neural network trained using the loss function $\mathcal{L}_{\text{MC}} + \mathcal{L}_{\text{EI}}$ successfully reconstructs images with a dynamic range similar to the original images, whereas the network trained with $\mathcal{L}_{\text{NMC}} + \mathcal{L}_{\text{EI}}$ as the loss function does not achieve this. However, both fail when the dynamic range of the original signal becomes excessively high. For signals with high dynamic range, characterized by a large norm $\|\cdot\|_2$, the network is unable to recover them as indicated in Theorem 1.

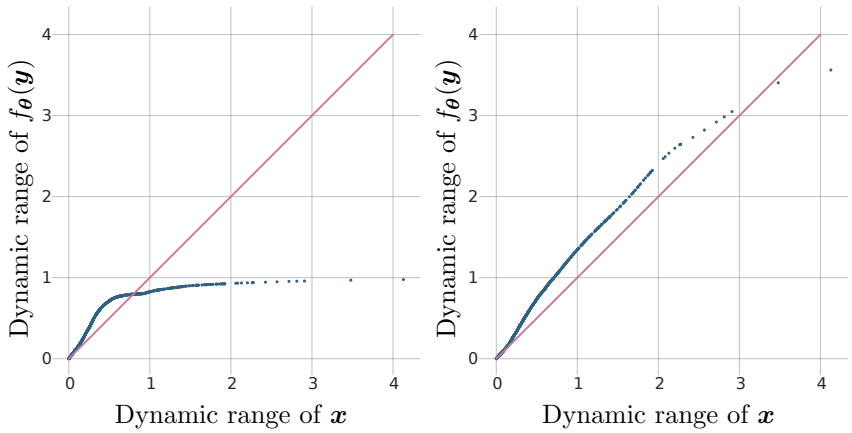

Figure 6: Plot of the dynamic range of $f_{\boldsymbol{\theta}}(\boldsymbol{y})$ depending on dynamic range of $\boldsymbol{x}$, where $\boldsymbol{y} = \eta(\boldsymbol{A}\boldsymbol{x})$. Left: The training is done with the losses $\mathcal{L}_{\text{NMC}} + \mathcal{L}_{\text{EI}}$. Right: The training is done with loss $\mathcal{L}_{\text{MC}} + \mathcal{L}_{\text{EI}}$. A perfect plot should be the identity line.

5.2.2 Synthetic dataset

First, we generate a random subspace of $\mathbb{R}^{100}$ with dimension $k \in \{1, \ldots, 100\}$ using basis vectors whose coordinates are drawn from a standard normal distribution. Next, we generate $N = 1000$ vectors $\{\boldsymbol{x}_i\}_{i=1}^N$ within this subspace, rescaling each vector such that a proportion $v \in (0, 1)$ of their components are clipped with the threshold μ set to 1.

We evaluate the recovery performance as a function of the parameters k and v. Figure 7 illustrates the network's ability to reconstruct unsaturated signals as these parameters vary. The performance decreases as the subspace dimension grows or the proportion of saturated samples increases. Indeed, signals from higher-dimensional subspaces are more challenging to reconstruct, which is consistent with the result of Theorem 1.

5.3 Audio

We evaluate the method on a real audio dataset. Specifically, we use the GTZAN dataset, which contains 10 genres (rock, classical, jazz, etc.), each represented by 100 audio files, all 30 seconds long with a sampling rate of 22,050 Hz. The audio signals are split into 30 segments of 1-second each and then saturated with a threshold level $\mu = 0.1$. Measurements $\boldsymbol{y}$ without any saturated entries are discarded. This process results in a training dataset of 21898 audio samples and a testing dataset of 100 samples.

The distribution of p_g is set uniformly on the interval $[0.1, 2]$. Results are compared with a state-of-the-art variational method called social sparsity (Zaviska et al., 2021; Siedenburg et al., 2014) and supervised methods. Both the supervised and self-supervised approaches use the same network architecture for training. We refer to the method trained using only 5% of the whole training dataset as "Supervised 5%", which is used to compare the performance of the both approaches under limited ground-truth data acquisition. We also compare our method with the following methods: unsupervised with loss $\mathcal{L}_{\text{MC}}$ alone, supervised with MSE + $\mathcal{L}_{\text{EI}}$. As shown in Table 1, the proposed self-supervised method achieves performance comparable

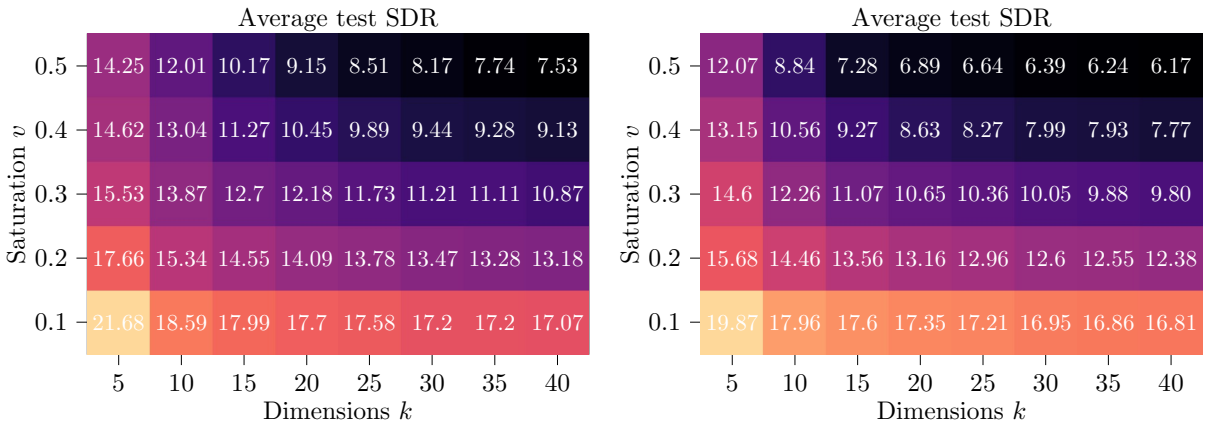

Figure 7: Average reconstruction performance as a function of saturated part v and signal set dimension k for both supervised (left) and self-supervised (right) methods. The value indicated corresponds to the mean SDR over the test dataset.

to the fully supervised approach, although the latter requires significantly less training time: 7 hour 46 mintutes compared to 13 hours 52 mintutes for the self-supervised method. The results further confirm that training with the MC loss alone does not yield additional information beyond the measurements themselves, as anticipated in Section 4. In addition, the supervised method with equivariance does not demonstrate any significant improvement over the standard supervised approach.

Table 1: Reconstruction performance, SDR and PESQ are averaged over all music test dataset.

Methods	SDR ↑	PESQ ↓
Identity	4.84 ± 2.12	2.7 ± 0.65
Social Sparsity	9.92 ± 4.46	2.09 ± 0.95
Supervised	11.69 ± 2.25	1.94 ± 0.75
Supervised 5%	9.79 ± 1.59	2.28 ± 0.78
Supervised + $\mathcal{L}_{\text{EI}}$	11.72 ± 2.23	1.92 ± 0.74
Proposed self-supervised	10.48 ± 2.20	2.20 ± 0.80
Unsupervised with $\mathcal{L}_{\text{MC}}$ alone	4.84 ± 2.12	2.68 ± 0.65
Proposed self-supervised with bias	9.27 ± 3.22	2.43 ± 0.90

To demonstrate that a supervised training dataset may not generalize well to a different test set, we conduct the following experiment: we create a supervised training dataset consisting of only music, while the test dataset includes both music and voice recordings (Vryzas et al., 2018a;b), with only measurement data available (no ground truth). The supervised method, trained using the MSE loss (2), learns solely from the training dataset, whereas the self-supervised method is trained on both the training and test datasets since it does not require ground truth. Both methods are then evaluated on the test dataset. The results, shown in Table 2, demonstrate that the self-supervised method is more robust when the training and test datasets differ.

Table 2: Average SDR performance on the test dataset, which includes both music and voice recordings.

Methods	SDR (dB)
Identity	6.54 ± 2.34
Supervised (trained on music)	10.94 ± 2.00
Proposed self-supervised (trained on music and voice)	11.92 ± 2.46

We also compare the self-supervised learning method to a supervised learning approach using diffusion models (Moliner et al., 2023). The comparison is conducted on a portion of the MAESTRO dataset (Hawthorne

Table 3: Average SDR and PESQ performance on the test MAESTRO dataset.

Methods	SDR ↑	PESQ ↓
Identity	5.00 ± 0	2.9 ± 0.73
Supervised	6.70 ± 1.69	2.22 ± 0.52
Proposed self-supervised	7.78 ± 8.64	2.47 ± 1.12

et al., 2019), used in Moliner's work, which consists of 200 hours of classical solo piano recordings. The measurement signals from Moliner et al. (2023) are used as a benchmark; although the saturation threshold varies for each signal, it consistently corresponds to an SDR value of 5. Each signal is then normalized to yield a saturation threshold of 0.1, while preserving a constant SDR of 5. This approach enables comparison between the proposed method, based on a fixed saturation threshold, and Moliner's trained method. Results demonstrate that the self-supervised method outperforms the supervised one Table 3. It is important to note that the proposed self-supervised method focuses on optimizing the distortion metric SDR, whereas this supervised method aims to optimize a perceptual metric PESQ. Results are then consistent with the perception-distortion tradeoff seen in Section 5.1.

5.4 HDR

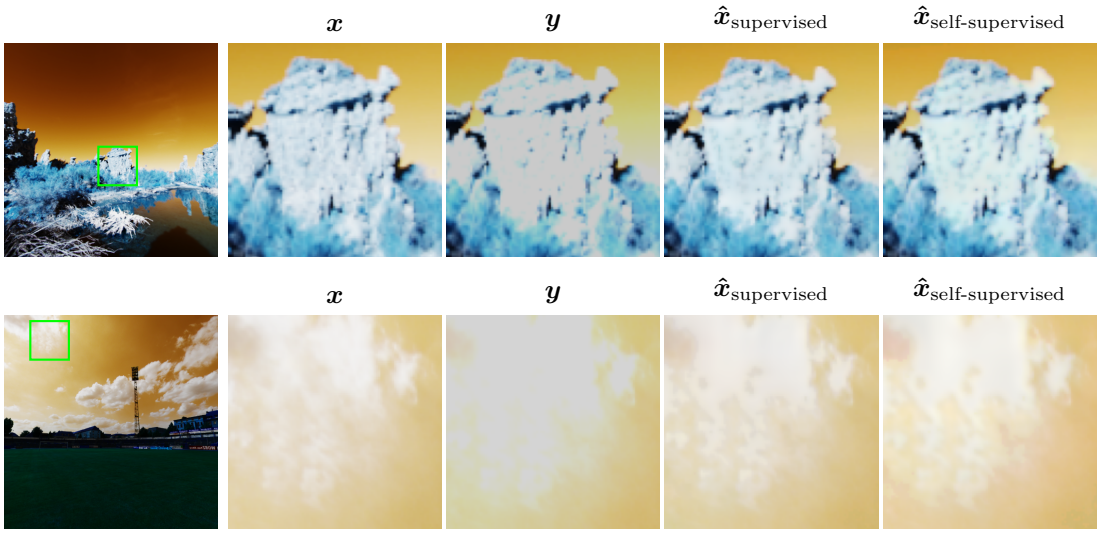

Figure 8: Image reconstruction on the test dataset. An exposition correction (Wikipedia) is applied to see details better.

The HDR experiment is inspired by Eilertsen et al. (2017), and its goal is to compare supervised and self-supervised methods. Results are summarized in Table 4 and in Figure 8. The dataset is composed of 1043 HDR images noted $\boldsymbol{u}$ (Le et al., 2023), which are considered as real scenes. Photos are taken with a virtual camera calibrated by a camera curve and exposure. For each image, we choose the exposure time to saturate between 5% and 15% of the pixels. We divide the image by the quantile q_v where v is chosen uniformly in $(0.85\ ,\ 0.95)$. Then we have $\mathbb{P}\left(\frac{\boldsymbol{u}}{q_v} > 1\right) = 1 - v$ if $\mathbb{P}$ is the cumulative histogram of $\boldsymbol{u}$. The camera curve is defined as

$$\omega(\boldsymbol{u})_j = (1+\sigma)\frac{u_j^\beta}{u_i^\beta + \sigma},$$

We use these functions to fit the database of real camera curves collected by Grossberg & Nayar (2003). We choose $\beta \sim \mathcal{N}(0.9, 0.1)$ and $\sigma \sim \mathcal{N}(0.6, 0.1)$. The images $\boldsymbol{x} = \omega\left(\frac{\boldsymbol{u}}{q_v}\right)$ represent the ground truth dataset. They are quantized and clipped to create the measurement dataset. This step is performed with

Equation (16):

$$y_j = \frac{\lfloor 255 \min(1, x_j) + 0.5 \rfloor}{255}. \tag{16}$$

We use an unfolded network with a U-Net architecture. It combines traditional iterative optimization with neural network learning. For each iteration, we replace a part of the optimization step with a neural network. We choose the Half-Quadratic Splitting (HQS) (Aggarwal et al., 2018) algorithm which aims to minimize $\varphi(x) + \lambda\psi(x)$, for φ and ψ two generic functions. The iteration step is given by:

$$u_k = \text{prox}_{\gamma\varphi}(x_k),$$
$$x_{k+1} = \text{prox}_{\sigma\lambda\psi}(u_k).$$

In our setting, φ corresponds to the measurement consistency term $\varphi(\boldsymbol{x}) = \|\rho(\boldsymbol{x}, \boldsymbol{y})\|^2$ and $\text{prox}_{\sigma\lambda\psi}(u_k)$ is replaced by a neural network. The proximal operator of the measurement consistency term is given by:

$$\text{prox}_{\gamma\varphi}(\boldsymbol{x})_j = \begin{cases} \frac{x_j + \gamma y_j}{1+\gamma} & \text{if} \quad |x_j| \leq \mu, \\ x_j & \text{otherwise} \end{cases}$$

for $j \in \{1, \ldots, n\}$.

Table 4: Reconstruction performance, PSNR is averaged over all test dataset images.

Methods	PSNR ↑	NIQE ↓
Identity	29.54 ± 6.95	4.21 ± 1.96
PnP DPIR	32.11 ± 5.80	4.06 ± 1.93
Supervised	36.67 ± 6.19	4.04 ± 1.74
Proposed self-supervised	35.04 ± 6.33	4.10 ± 1.85

In Table 4, we compare our method against two reference approaches: the supervised method from Eilertsen et al. (2017) and the Plug-and-Play (PnP) method (Venkatakrishnan et al., 2013). The PnP method is an iterative technique that integrates a denoising module into the optimization process, replacing the proximal operator. We used the Deep Plug-and-Play Image Restoration (DPIR) method (Zhang et al., 2021), a PnP approach based on HQS in which the denoising network is a pre-trained DRUNet, and the noise level for the denoiser is adapted at each iteration. For better results, we modified the initialization of the algorithm – which is generally set to $\boldsymbol{y}$ – by adding a white Gaussian noise of standard deviation $\sigma = 0.18$, which we found to better avoid local minima close to $\boldsymbol{y}$. In this way, DPIR outperforms the other PnP methods tested. Results in Table 4, demonstrate that the self-supervised method performs on par with the supervised method and significantly outperforms the DPIR approach. As illustrated in Figure 8, both the supervised and self-supervised methods effectively recover details in the images.

6 Conclusion

In this study, we propose a self-supervised method that uses amplitude invariance to address the nonlinear declipping problem. We provide a theoretical framework with guarantees for model identification of scale invariant signal models and unique recovery of the unsaturated signals when the operator involves random matrices with coefficients following a Gaussian distribution. Experimental results, carried out on audio and images, indicate that this method can perform on par with the supervised approach, and surpasses variational methods. This work opens up new possibilities for learning-based methods in nonlinear inverse problems.

References

Hemant K Aggarwal, Merry P Mani, and Mathews Jacob. MoDL: Model-based deep learning architecture for inverse problems. *IEEE transactions on medical imaging*, 38(2):394–405, 2018.

Ali Ahmed, Benjamin Recht, and Justin Romberg. Blind deconvolution using convex programming. *IEEE Transactions on Information Theory*, 60(3):1711–1732, 2013.

anonymous author. Equivariance-based self-supervised learning for audio signal recovery from clipped measurements. In *2024 32nd European Signal Processing Conference (EUSIPCO)*, pp. 852–856. IEEE, 2024.

Chinmay Belthangady and Loic A. Royer. Applications, Promises, and Pitfalls of Deep Learning for Fluorescence Image Reconstruction, February 2019.

Yochai Blau and Tomer Michaeli. The Perception-Distortion Tradeoff. In *2018 IEEE/CVF Conference on Computer Vision and Pattern Recognition*, pp. 6228–6237, June 2018.

Stephen P Boyd and Lieven Vandenberghe. *Convex optimization*. Cambridge university press, 2004.

E.J. Candes and M.B. Wakin. An Introduction To Compressive Sampling. *IEEE Signal Processing Magazine*, 25(2):21–30, March 2008. ISSN 1053-5888.

Dongdong Chen, Julián Tachella, and Mike E. Davies. Equivariant Imaging: Learning Beyond the Range Space. In *Proceedings of the IEEE/CVF International Conference on Computer Vision*, pp. 4379–4388, August 2021.

Yuxin Chen, Yuejie Chi, and Andrea J Goldsmith. Exact and Stable Covariance Estimation from Quadratic Sampling via Convex Programming. *IEEE Transactions on Information Theory*, 61(7):4034–4059, 2015.

Kebin Contreras, Brayan Monroy, and Jorge Luis Bacca. High dynamic range modulo imaging for robust object detection in autonomous driving. In *ROAM ECCV 2024*.

Giannis Daras, Kulin Shah, Yuval Dagan, Aravind Gollakota, Alex Dimakis, and Adam Klivans. Ambient diffusion: Learning clean distributions from corrupted data. *Advances in Neural Information Processing Systems*, 36:288–313, 2023.

Bruno Defraene, Naim Mansour, Steven De Hertogh, Toon Van Waterschoot, Moritz Diehl, and Marc Moonen. Declipping of audio signals using perceptual compressed sensing. *IEEE Transactions on Audio, Speech, and Language Processing*, 21(12):2627–2637, 2013.

Gabriel Eilertsen, Joel Kronander, Gyorgy Denes, Rafał K. Mantiuk, and Jonas Unger. HDR image reconstruction from a single exposure using deep CNNs. *ACM Transactions on Graphics*, 36(6):1–15, December 2017. ISSN 0730-0301, 1557-7368.

Kenneth Falconer. *Fractal geometry: mathematical foundations and applications*. John Wiley & Sons, 2013.

Simon Foucart and Tom Needham. Sparse recovery from saturated measurements. *Information and Inference*, pp. iaw020, December 2016. ISSN 2049-8764, 2049-8772.

Clément Gaultier, Nancy Bertin, and Rémi Gribonval. Cascade: Channel-aware structured cosparse audio declipper. In *2018 IEEE International Conference on Acoustics, Speech and Signal Processing (ICASSP)*, pp. 571–575. IEEE, 2018.

Clément Gaultier, Srđjan Kitić, Rémi Gribonval, and Nancy Bertin. Sparsity-based audio declipping methods: Selected overview, new algorithms, and large-scale evaluation. *IEEE/ACM Transactions on Audio, Speech, and Language Processing*, 29:1174–1187, 2021.

Sivan Gleichman and Yonina C Eldar. Blind compressed sensing. *IEEE Transactions on Information Theory*, 57(10):6958–6975, 2011.

Michael Grossberg and S.K. Nayar. What is the Space of Camera Response Functions? In *2003 IEEE Computer Society Conference on Computer Vision and Pattern Recognition, 2003. Proceedings.*, volume 2, pp. II – 602. IEEE, July 2003.

Curtis Hawthorne, Andriy Stasyuk, Adam Roberts, Ian Simon, Cheng-Zhi Anna Huang, Sander Dieleman, Erich Elsen, Jesse Engel, and Douglas Eck. Enabling factorized piano music modeling and generation with the MAESTRO dataset. In *International Conference on Learning Representations*, 2019.

Kyong Hwan Jin, Michael T McCann, and Michael Unser. Bpconvnet for compressed sensing recovery in bioimaging. 2016.

Srdjan Kitic, Laurent Jacques, Nilesh Madhu, Michael Peter Hopwood, Ann Spriet, and Christophe De Vleeschouwer. Consistent Iterative Hard Thresholding for Signal Declipping. In *Acoustics, Speech and Signal Processing (ICASSP), 2013 IEEE International Conference on*. IEEE, 2013.

Alexander Krull, Tim-Oliver Buchholz, and Florian Jug. Noise2void-learning denoising from single noisy images. In *Proceedings of the IEEE/CVF conference on computer vision and pattern recognition*, pp. 2129–2137, 2019.

Phuoc-Hieu Le, Quynh Le, Rang Nguyen, and Binh-Son Hua. Single-Image HDR Reconstruction by Multi-Exposure Generation. In *Proceedings of the IEEE/CVF Winter Conference on Applications of Computer Vision (WACV)*, January 2023.

Jaakko Lehtinen, Jacob Munkberg, Jon Hasselgren, Samuli Laine, Tero Karras, Miika Aittala, and Timo Aila. Noise2Noise: Learning image restoration without clean data. *International Conference on Machine Learning*, 2018.

Michael Lustig, David Donoho, and John M Pauly. Sparse MRI: The application of compressed sensing for rapid MR imaging. *Magnetic Resonance in Medicine: An Official Journal of the International Society for Magnetic Resonance in Medicine*, 58(6):1182–1195, 2007.

Tom Mertens, Jan Kautz, and Frank Van Reeth. Exposure Fusion. In *15th Pacific Conference on Computer Graphics and Applications (PG'07)*, pp. 382–390, Maui, HI, October 2007. IEEE. ISBN 978-0-7695-3009-3.

Francesco Mezzadri. How to generate random matrices from the classical compact groups. volume 54, pp. 592 – 604, February 2007.

Sreyas Mohan, Zahra Kadkhodaie, Eero P. Simoncelli, and Carlos Fernandez-Granda. Robust and interpretable blind image denoising via bias-free convolutional neural networks. In *International Conference on Learning Representations*, February 2020.

Eloi Moliner, Jaakko Lehtinen, and Vesa Välimäki. Solving Audio Inverse Problems with a Diffusion Model. In *ICASSP 2023-2023 IEEE International Conference on Acoustics, Speech and Signal Processing (ICASSP)*. IEEE, March 2023.

Alexey Ozerov, Çağdaş Bilen, and Patrick Pérez. Multichannel audio declipping. In *2016 IEEE International Conference on Acoustics, Speech and Signal Processing (ICASSP)*, pp. 659–663. IEEE, 2016.

Gilles Puy, Mike E. Davies, and Remi Gribonval. Recipes for Stable Linear Embeddings From Hilbert Spaces to $\mathbb{R}^m$. *IEEE Transactions on Information Theory*, 63(4):2171–2187, April 2017. ISSN 0018-9448, 1557-9654.

James C Robinson. *Dimensions, embeddings, and attractors*, volume 186. Cambridge University Press, 2010.

Olaf Ronneberger, Philipp Fischer, and Thomas Brox. U-net: Convolutional networks for biomedical image segmentation. In *Medical image computing and computer-assisted intervention–MICCAI 2015: 18th international conference, Munich, Germany, October 5-9, 2015, proceedings, part III 18*, pp. 234–241. Springer, 2015.

Leonid I Rudin, Stanley Osher, and Emad Fatemi. Nonlinear total variation based noise removal algorithms. *Physica D: nonlinear phenomena*, 60(1-4):259–268, 1992.

Tim Sauer, James A. Yorke, and Martin Casdagli. Embedology. *Journal of Statistical Physics*, 65(3-4): 579–616, November 1991.

Jérémy Scanvic, Mike Davies, Patrice Abry, and Julián Tachella. Self-Supervised Learning for Image Super-Resolution and Deblurring, March 2024.

Yoav Shechtman, Yonina C. Eldar, Oren Cohen, Henry Nicholas Chapman, Jianwei Miao, and Mordechai Segev. Phase Retrieval with Application to Optical Imaging: A contemporary overview. *IEEE Signal Processing Magazine*, 32(3):87–109, May 2015. ISSN 1053-5888.

Kai Siedenburg, Matthieu Kowalski, and Monika Dorfler. Audio declipping with social sparsity. In *2014 IEEE International Conference on Acoustics, Speech and Signal Processing (ICASSP)*, pp. 1577–1581, Florence, Italy, May 2014. IEEE. ISBN 978-1-4799-2893-4.

Julián Tachella and Laurent Jacques. Learning to reconstruct signals from binary measurements. In *Fourteenth International Conference on Sampling Theory and Applications*, 2023.

Julián Tachella, Dongdong Chen, and Mike Davies. Sensing theorems for unsupervised learning in linear inverse problems. *Journal of Machine Learning Research*, 24(39):1–45, 2023.

Singanallur V Venkatakrishnan, Charles A Bouman, and Brendt Wohlberg. Plug-and-play priors for model based reconstruction. In *2013 IEEE global conference on signal and information processing*, pp. 945–948. IEEE, 2013.

Roman Vershynin. *High-dimensional probability: An introduction with applications in data science*, volume 47. Cambridge university press, 2018.

Nikolaos Vryzas, Rigas Kotsakis, Aikaterini Liatsou, Charalampos A Dimoulas, and George Kalliris. Speech emotion recognition for performance interaction. *Journal of the Audio Engineering Society*, 66(6):457–467, 2018a.

Nikolaos Vryzas, Maria Matsiola, Rigas Kotsakis, Charalampos Dimoulas, and George Kalliris. Subjective evaluation of a speech emotion recognition interaction framework. In *Proceedings of the Audio Mostly 2018 on Sound in Immersion and Emotion*, pp. 1–7. 2018b.

Wikipedia. Exposure value. `https://en.wikipedia.org/wiki/Exposure_value`.

Pavel Zaviska, Pavel Rajmic, Alexey Ozerov, and Lucas Rencker. A Survey and an Extensive Evaluation of Popular Audio Declipping Methods. *IEEE Journal of Selected Topics in Signal Processing*, 15(1):5–24, January 2021. ISSN 1932-4553, 1941-0484.

Kai Zhang, Yawei Li, Wangmeng Zuo, Lei Zhang, Luc Van Gool, and Radu Timofte. Plug-and-play image restoration with deep denoiser prior. *IEEE Transactions on Pattern Analysis and Machine Intelligence*, 44(10):6360–6376, 2021.

A Appendix: Proof of Thm 1

We recall that the idea of the proof is to upper-bound two probabilities: *(i)* the probability that the number of common unsaturated measurements is small; *(ii)* the probability that two signals have the same common unsaturated measurements given that the number of saturated measurements is low. Before we begin, we need to introduce some tools of linear embedding. Theorem 2 allows us to prove Corollary 2.1 used to control the first targeted probability. Theorem 3 is used to control the second one. We also recall the Hoeffding inequality for sub-Gaussian random variables, which we will use to verify an assumption for Theorem 2.

Lemma 1. ***Hoeffding inequality***. *Let $X_1, \dots, X_m$ be independent random variables, where X_i has mean μ_i and is σ_i-sub-Gaussian. Then for all $t \geq 0$ we have*

$$\mathbb{P}\left(\left| \sum_{i=0}^{m} X_i - \mu_i \right| \geq t \right) \leq 2 \exp\left(- \frac{t^2}{2 \sum\limits_{i=0}^{m} \sigma_i^2} \right)$$

Theorem 2. *This theorem is adapted from Puy et al. (2017, Theorem II.2).*
Let us assume that the normalized set $S_{\mathcal{X}}$ has a finite upper box-counting dimension $\dim(S_{\mathcal{X}})$ which is strictly bounded by $k \geq 1$ i.e. $\dim(S_{\mathcal{X}}) < k$, and so there exists a signal set dependent constant $\epsilon^* \in \left(0, \frac{1}{2}\right)$ such that $N_{S_{\mathcal{X}}}(\epsilon) \leq \epsilon^{-k}$ for all $\epsilon \leq \epsilon^*$. Let $A : R^n \to \mathbb{R}^m$ such that $A_{ij} \sim \mathcal{N}\left(0, \frac{1}{m}\right)$. Then there exists $c_1 > 0$ such that, for any $\xi, \delta \in (0,1)$, we have $\sup_{\boldsymbol{x} \in S_{\mathcal{X}}} |c\|\boldsymbol{A}\boldsymbol{x}\|_1 - 1| \leq \delta$ with probability at least $1 - \xi$ provided that

$$m \geq \frac{C_1}{c_1 \delta^2} \max\left(k \log\left(\frac{1}{\epsilon^*}\right), \log\left(\frac{6}{\xi}\right)\right),$$

where C_1 is an absolute constant.

The proof of Theorem 2 closely follows that of Puy et al. (2017, Theorem II.2), which uses a general chaining argument. For more detail see Vershynin (2018, Chapter 8). We still need to prove the following lemma:

Lemma 2. *Let $c > 0$ and h define as*

$$\begin{array}{rccl} h: & \mathbb{R}^n & \to & \mathbb{R} \\ & \boldsymbol{x} & \mapsto & c\|\boldsymbol{A}\boldsymbol{x}\|_1 - \|\boldsymbol{x}\|_2. \end{array}$$

Then there exist a constant $c_1 \in \mathbb{R}^+$ such that for any fixed $\boldsymbol{u}, \boldsymbol{v} \in S_{\mathcal{X}} \cup \{\boldsymbol{0}\}$,

$$\mathbb{P}\left(|h(\boldsymbol{u}) - h(\boldsymbol{v})| \geq \lambda\|\boldsymbol{u} - \boldsymbol{v}\|\right) \leq 2e^{-c_1 m \lambda^2} \quad \forall \lambda \in \mathbb{R}^+.$$

Proof. We consider $h : \boldsymbol{x} \mapsto c\|\boldsymbol{A}\boldsymbol{x}\|_1 - \|\boldsymbol{x}\|_2$ with $c > 0$. Restricted to $S_{\mathcal{X}}$, we have $h : \boldsymbol{x} \mapsto c\|\boldsymbol{A}\boldsymbol{x}\|_1 - 1$.

$$\begin{aligned} &\mathbb{P}\left(|h(\boldsymbol{u}) - h(\boldsymbol{v})| \geq \lambda\|\boldsymbol{u} - \boldsymbol{v}\|\right) && (17) \\ &= \mathbb{P}(c|\|\boldsymbol{A}\boldsymbol{u}\|_1 - \|\boldsymbol{A}\boldsymbol{v}\|_1| \geq \lambda\|\boldsymbol{u} - \boldsymbol{v}\|) \\ &= \mathbb{P}\left(c\left|\sum_{i=0}^{m} |\boldsymbol{a}_i^\top \boldsymbol{u}| - |\boldsymbol{a}_i^\top \boldsymbol{v}|\right| \geq \lambda\|\boldsymbol{u} - \boldsymbol{v}\|\right). && (18) \end{aligned}$$

We note $X_i = |\boldsymbol{a}_i^\top \boldsymbol{u}| - |\boldsymbol{a}_i^\top \boldsymbol{v}|$. Let's show that X_i is sub-Gaussian: For all $q \in \mathbb{N}$ and for all $i \in \{1, \ldots, m\}$,

$$\mathbb{E}\left[|X_i|^q\right] = E\left[\left||\boldsymbol{a}_i^\top \boldsymbol{u}| - |\boldsymbol{a}_i^\top \boldsymbol{v}|\right|^q\right] \leq E[|\boldsymbol{a}_i^\top (\boldsymbol{u} - \boldsymbol{v})|^q]$$

by the reverse triangle inequality. As

$$\boldsymbol{a}_i^\top (\boldsymbol{u} - \boldsymbol{v}) \sim \mathcal{N}\left(0, \frac{\|\boldsymbol{u} - \boldsymbol{v}\|_2^2}{m}\right),$$

$\boldsymbol{a}_i^\top (\boldsymbol{u} - \boldsymbol{v})$ is Gaussian and thus X_i is also sub-Gaussian with parameter $\sigma_i^2 \leq \frac{\|\boldsymbol{u} - \boldsymbol{v}\|_2^2}{m}$. We can therefore apply the Lemma 1:

$$\mathbb{P}\left(c\left|\sum_{i=0}^{m} X_i\right| > t\right) \leq 2\exp\left(-\frac{t^2}{2c^2 \sum_{i=0}^{m} \sigma_i^2}\right)$$

and thus give an upper bound of Equation (18):

$$\begin{aligned} &\mathbb{P}(|h(\boldsymbol{u}) - h(\boldsymbol{v})| \geq \lambda\|\boldsymbol{u} - \boldsymbol{v}\|) \\ &\leq 2\exp\left(-\frac{(\lambda\|\boldsymbol{u} - \boldsymbol{v}\|)^2}{2c^2 \sum_{i=0}^{m} \sigma_i^2}\right) \\ &\leq 2\exp\left(-\frac{(\lambda\|\boldsymbol{u} - \boldsymbol{v}\|)^2}{2c^2 \sum_{i=0}^{m} \frac{\|\boldsymbol{u} - \boldsymbol{v}\|_2^2}{m}}\right) \\ &\leq 2\exp\left(-\frac{\lambda^2}{2c^2}\right) \\ &= 2\exp\left(-mc_1\lambda^2\right). \end{aligned}$$

We conclude the proof with $c_1 = \dfrac{1}{2mc^2}$. □

Corollary 2.1. *Under assumptions of Theorem 2, we have for all* $m \geq k \log\left(\dfrac{1}{\epsilon^*}\right)$*:*

$$\mathbb{P}\big(\forall \boldsymbol{x} \in \mathcal{X} : \|\boldsymbol{A}\boldsymbol{x}\|_1 \leq \sqrt{m}\|\boldsymbol{x}\|_2\big) > 1 - 6e^{-Cm}.$$

Proof. By applying Theorem 2 for $c = \frac{2}{\sqrt{m}}$ we deduce that with $c_1 = \frac{1}{2mc^2} = \frac{1}{8}$, for any $\xi, \delta \in (0,1)$, we have with probability $1-\xi$,

$$\forall \boldsymbol{z} \in S_{\mathcal{X}}, \quad \left|\frac{2}{\sqrt{m}}\|\boldsymbol{A}\boldsymbol{z}\|_1 - 1\right| \leq \delta \tag{19}$$

as long as

$$m \geq \frac{C_1}{c_1\delta^2} \max\left(k\log\left(\frac{1}{\epsilon^*}\right), \log\left(\frac{6}{\xi}\right)\right).$$

For all $\boldsymbol{x} \in \mathcal{X}$, we obtain by replacing $\boldsymbol{z}$ by $\frac{\boldsymbol{x}}{\|\boldsymbol{x}\|}$ in Equation (19),

$$\|\boldsymbol{A}\boldsymbol{x}\|_1 \leq (\delta+1)\frac{\sqrt{m}}{2}\|\boldsymbol{x}\|_2 \tag{20}$$

provided that

$$m \geq \frac{8C_1}{\delta^2} \max\left(k\log\left(\frac{1}{\epsilon^*}\right), \log\left(\frac{6}{\xi}\right)\right).$$

By setting $C = \frac{1}{8C_1}$, $\delta = 1$ and $\xi = 6\exp\big(-Cm\big)$, we can verify that the last inequality holds for all $m \geq k\log\left(\dfrac{1}{\epsilon^*}\right)$ and thus:

$$\mathbb{P}\big(\forall \boldsymbol{x} \in \mathcal{X} : \|\boldsymbol{A}\boldsymbol{x}\|_1 \leq \sqrt{m}\|\boldsymbol{x}\|_2\big) > 1 - 6e^{-Cm}.$$

□

Theorem 3. *Adapted from Robinson (2010, Thm. 4.3) Let a compact set* $\mathcal{X}$ *with finite upper box-counting dimension* $\dim(\mathcal{X}) < k$ *and* $\boldsymbol{A} \in \mathbb{R}^{m\times n}$ *such that* $A_{ij} \sim \mathcal{N}\left(0, \frac{1}{m}\right)$*. If* $m > 2k$ *then*

$$\mathbb{P}\left(\boldsymbol{A}\boldsymbol{x} = \boldsymbol{A}\boldsymbol{u} \text{ for some } \boldsymbol{x} \neq \boldsymbol{u} \in \mathcal{X}\right) = 0$$

Note that Robinson's theorem states that almost every linear map $L\colon \mathbb{R}^N \to \mathbb{R}^k$ (for $m > 2k$) embeds $\mathcal{X}$ injectively with Hölder distortion $|\boldsymbol{x}-\boldsymbol{y}| \leq C|L\boldsymbol{x} - L\boldsymbol{y}|^\alpha$. By considering the definition of "almost every" in the sense of measure, we can say that the set of non-injective linear maps has zero measure, and therefore zero probability.

For the rest of the proof, we will consider

$$\mathcal{X}_R = \mathcal{X} \cap \mathbb{B}_{\|\cdot\|_2}\left(0, \sqrt{m}\mu\alpha\right)$$

with $R = \sqrt{m}\mu\alpha$ and $\alpha > 0$ to be define latter. We define

$$\mathcal{I}_{\text{sat}}(\boldsymbol{y}) = \{j : |y_j| \geq \mu\}$$
$$\overline{\mathcal{I}_{\text{sat}}}(\boldsymbol{y}) = \{j : |y_j| < \mu\}$$

as the sets of the index of respectively unsaturated and saturated entries of $\boldsymbol{y}$. We note $\boldsymbol{A}^{\mathcal{I}}$ the matrix represents the row-submatrix of A where only the rows indexed by $\mathcal{I}$ are selected.

Let $\mathcal{I}^{\boldsymbol{A}}_{\boldsymbol{x},\boldsymbol{u}} = \overline{\mathcal{I}_{\text{sat}}}(\boldsymbol{A}\boldsymbol{x}) \cap \overline{\mathcal{I}_{\text{sat}}}(\boldsymbol{A}\boldsymbol{u})$ be the intersection of the unsaturated index sets of $\boldsymbol{A}\boldsymbol{x}$ and $\boldsymbol{A}\boldsymbol{u}$. Using the law of total probability we can decompose the probability of Theorem 1 into the two target probabilities. By considering:

$$\mathcal{A} = \left\{\exists \boldsymbol{x}, \boldsymbol{u} \in \mathcal{X}_R, \boldsymbol{x} \neq \boldsymbol{u} : \boldsymbol{A}^{\mathcal{I}^{\boldsymbol{A}}_{\boldsymbol{x},\boldsymbol{u}}}\boldsymbol{x} = \boldsymbol{A}^{\mathcal{I}^{\boldsymbol{A}}_{\boldsymbol{x},\boldsymbol{u}}}\boldsymbol{u}\right\}$$
$$\mathcal{B} = \left\{\forall \boldsymbol{x}, \boldsymbol{u} \in \mathcal{X}_R, \boldsymbol{x} \neq \boldsymbol{u} : \left|\mathcal{I}^{\boldsymbol{A}}_{\boldsymbol{x},\boldsymbol{u}}\right| > (1-2\alpha)m\right\}$$

where $\mathcal{A}$ is the set of events where there exists two signals having the same common unsaturated measurements, $\mathcal{B}$ is the set of events where the number of common unsaturated measurements is greater than $(1-2\alpha)m$ for all couple of signals. And taking it into the law of total probability:

$$\begin{aligned}\mathbb{P}(\mathcal{A}) &= \mathbb{P}(\mathcal{A} \cap \mathcal{B}) + \mathbb{P}\left(\mathcal{A} \cap \bar{\mathcal{B}}\right) \\ &= \mathbb{P}(\mathcal{A} \mid \mathcal{B}) \times \mathbb{P}(\mathcal{B}) + \mathbb{P}\left(\mathcal{A} \mid \bar{\mathcal{B}}\right) \times \mathbb{P}\left(\bar{\mathcal{B}}\right) \\ &\leq \mathbb{P}(\mathcal{A} \mid \mathcal{B}) + \mathbb{P}\left(\bar{\mathcal{B}}\right) \end{aligned} \tag{21}$$

as we have that $\mathbb{P}(\mathcal{B}) < 1$ and $\mathbb{P}\left(\mathcal{A}|\bar{\mathcal{B}}\right) < 1$.

$\mathbb{P}(\mathcal{A} \mid \mathcal{B})$ and $\mathbb{P}\left(\bar{\mathcal{B}}\right)$ are respectively the probability that two signals have the same common unsaturated measurements given that the number of saturated measurements is low, and the probability there exist two distinct signals whose the number of common unsaturated measurements is low. Next, we upper-bound separately the two terms $\mathbb{P}(\mathcal{A} \mid \mathcal{B})$ and $\mathbb{P}\left(\bar{\mathcal{B}}\right)$. We start with the first one:

$$\begin{aligned}\mathbb{P}\big(\mathcal{A} \mid \mathcal{B}\big) &= \mathbb{P}\left(\left\{\exists \boldsymbol{x}, \boldsymbol{u} \in \mathcal{X}_R, \boldsymbol{x} \neq \boldsymbol{u} : \boldsymbol{A}^{\mathcal{I}^{\boldsymbol{A}}_{\boldsymbol{x},\boldsymbol{u}}}\boldsymbol{x} = \boldsymbol{A}^{\mathcal{I}^{\boldsymbol{A}}_{\boldsymbol{x},\boldsymbol{u}}}\boldsymbol{u}\right\} \middle| \left\{\forall \boldsymbol{x}, \boldsymbol{u} \in \mathcal{X}_R, \boldsymbol{x} \neq \boldsymbol{u} : |\mathcal{I}^{\boldsymbol{A}}_{\boldsymbol{x},\boldsymbol{u}}| > (1-2\alpha)m\right\}\right) \\ &\leq \mathbb{P}\Big(\exists\, \mathcal{I} \subset [\![0:m]\!],\, |\mathcal{I}| > (1-2\alpha)m,\ \exists \boldsymbol{x}, \boldsymbol{u} \in \mathcal{X}_R, \boldsymbol{x} \neq \boldsymbol{u} : \boldsymbol{A}^{\mathcal{I}}\boldsymbol{x} = \boldsymbol{A}^{\mathcal{I}}\boldsymbol{u}\Big).\end{aligned}$$

And because of $\mathcal{X}$ is a cone, we have (Robinson, 2010):

$$\dim(\mathcal{X}_R) \leq \dim(\mathcal{X} \cap \mathbb{S}) + 1 = \dim(S_{\mathcal{X}}) + 1 < k + 1$$

We thus have, as long as $(1-2\alpha)m > 2(k+1)$, and thanks to Theorem 3:

$$\mathbb{P}\left(\exists\, \mathcal{I} \subset [\![0:m]\!], |\mathcal{I}| > (1-2\alpha)m,\, \exists \boldsymbol{x}, \boldsymbol{u} \in \mathcal{X}_R, \boldsymbol{x} \neq \boldsymbol{u} : \boldsymbol{A}^{\mathcal{I}}\boldsymbol{x} = \boldsymbol{A}^{\mathcal{I}}\boldsymbol{u}\right) = 0 \tag{22}$$

And so the first right-hand side term of Equation (21) is equals 0.

From $(1-2\alpha)m > 2(k+1)$ which imposes $\alpha < \frac{1}{2} - \frac{k+1}{m}$, we can fix α and therefore fix $R < \sqrt{m}\mu\left(\frac{1}{2} - \frac{k+1}{m}\right)$. We also note as $\alpha > 0$, we necessarily have $2(k+1) < m$.
We can now upper-bound the second term appearing in Equation (21):

$$\mathbb{P}\big(\exists \boldsymbol{x}, \boldsymbol{u} \in \mathcal{X}_R, \boldsymbol{x} \neq \boldsymbol{u} : \left|\mathcal{I}^{\boldsymbol{A}}_{\boldsymbol{x},\boldsymbol{u}}\right| \leq (1-2\alpha)m\big).$$

By observing that for two set I and J of $\{1, \ldots, m\}$ with $|I \cap J| \leq (1-2\alpha)m$, this means that $\left|\bar{I} \cup \bar{J}\right| > 2\alpha m$, which implies that either $\left|\bar{I}\right| > \alpha m$ or $\left|\bar{J}\right| > \alpha m$ (since otherwise the union has size $< 2\alpha m$), therefore $|I| \leq (1-\alpha)m$ or $|J| \leq (1-\alpha)m$, we can deduce:

$$\begin{aligned}&\left|\mathcal{I}^{\boldsymbol{A}}_{\boldsymbol{x},\boldsymbol{u}}\right| \leq (1-2\alpha)m \\ \Leftrightarrow &\left|\overline{\mathcal{I}_{\text{sat}}}(\boldsymbol{A}\boldsymbol{x}) \cap \overline{\mathcal{I}_{\text{sat}}}(\boldsymbol{A}\boldsymbol{u})\right| \leq (1-2\alpha)m \\ \Rightarrow &\begin{cases} \left|\overline{\mathcal{I}_{\text{sat}}}(\boldsymbol{A}\boldsymbol{x})\right| \leq \left\lfloor \frac{m+(1-2\alpha)m}{2} \right\rfloor \leq (1-\alpha)m \\ \text{or} \\ \left|\overline{\mathcal{I}_{\text{sat}}}(\boldsymbol{A}\boldsymbol{u})\right| \leq \left\lfloor \frac{m+(1-2\alpha)m}{2} \right\rfloor \leq (1-\alpha)m \end{cases}\end{aligned}$$

we have

$$\begin{aligned}
&\mathbb{P}\left(\exists \boldsymbol{x}, \boldsymbol{u} \in \mathcal{X}_R, \boldsymbol{x} \neq \boldsymbol{u} : |\mathcal{I}^{\boldsymbol{A}}_{\boldsymbol{x},\boldsymbol{u}}| \leq (1-2\alpha)m\right) \\
&\leq \mathbb{P}\left(\left\{\exists \boldsymbol{x} \in \mathcal{X}_R : \left|\overline{\mathcal{I}_{\text{sat}}}(\boldsymbol{A}\boldsymbol{x})\right| \leq (1-\alpha)m\right\} \cup \left\{\exists \boldsymbol{u} \in \mathcal{X}_R : \left|\overline{\mathcal{I}_{\text{sat}}}(\boldsymbol{A}\boldsymbol{u})\right| \leq (1-\alpha)m\right\}\right) \\
&\leq 2\mathbb{P}\left(\exists \boldsymbol{x} \in \mathcal{X}_R : \left|\overline{\mathcal{I}_{\text{sat}}}(\boldsymbol{A}\boldsymbol{x})\right| \leq (1-\alpha)m\right)
\end{aligned}$$

and if we remark that

$$\|\boldsymbol{A}\boldsymbol{x}\|_1 = \sum_{i=1}^{m} |\boldsymbol{a}_{ix}^\top| \geq \sum_{i \in \mathcal{I}_{\text{sat}}(\boldsymbol{A}\boldsymbol{x})} |\boldsymbol{a}_{ix}^\top| \geq \sum_{i \in \mathcal{I}_{\text{sat}}(\boldsymbol{A}\boldsymbol{x})} \mu$$

we obtain

$$\|\boldsymbol{A}\boldsymbol{x}\|_1 \geq |\mathcal{I}_{\text{sat}}(\boldsymbol{A}\boldsymbol{x})|\, \mu.$$

Thanks to Corollary 2.1 we know that with probability at least $1 - 6e^{-Cm}$,

$$\|\boldsymbol{A}\boldsymbol{x}\|_1 \leq \sqrt{m}\|\boldsymbol{x}\|_2 \leq m\alpha\mu.$$

We deduce from these two last inequalities

$$\begin{aligned}
|\mathcal{I}_{\text{sat}}(\boldsymbol{A}\boldsymbol{x})|\, \mu &\leq m\alpha\mu \\
m - \left|\overline{\mathcal{I}_{\text{sat}}}(\boldsymbol{A}\boldsymbol{x})\right| &\leq m\alpha \\
(1-\alpha)m &\leq \left|\overline{\mathcal{I}_{\text{sat}}}(\boldsymbol{A}\boldsymbol{x})\right|.
\end{aligned}$$

And thus

$$\mathbb{P}\left(\exists \boldsymbol{x} \in \mathcal{X}_R : \left|\overline{\mathcal{I}_{\text{sat}}}(\boldsymbol{A}\boldsymbol{x})\right| \leq (1-\alpha)m\right) \leq 6e^{-Cm}$$

as long as

$$m \geq k \log\left(\frac{1}{\epsilon^*}\right).$$

Finally,

$$\mathbb{P}\left(\bar{\mathcal{B}}\right) \leq 12e^{-Cm}. \tag{23}$$

we conclude by adding the upper-bound obtain in Equation (22) and Equation (23):

$$\begin{aligned}
\mathbb{P}\left(\exists \boldsymbol{x}, \boldsymbol{u} \in \mathcal{X}_R, \boldsymbol{x} \neq \boldsymbol{u} : \eta(\boldsymbol{A}\boldsymbol{x}) = \eta\left(\boldsymbol{A}\boldsymbol{u}\right)\right) &\leq \mathbb{P}\left(\exists \boldsymbol{x}, \boldsymbol{u} \in \mathcal{X}_R, \boldsymbol{x} \neq \boldsymbol{u} : \boldsymbol{A}^{\mathcal{I}^{\boldsymbol{A}}_{\boldsymbol{x},\boldsymbol{u}}}\boldsymbol{x} = \boldsymbol{A}^{\mathcal{I}^{\boldsymbol{A}}_{\boldsymbol{x},\boldsymbol{u}}}\boldsymbol{u}\right) \\
&\leq \mathbb{P}\left(\mathcal{A} \mid \mathcal{B}\right) + \mathbb{P}\left(\bar{\mathcal{B}}\right) \\
&\leq 0 + 12e^{-Cm}.
\end{aligned}$$

B Appendix: Hyperparameters and training details

Table 5: Hyperparameters for different experiments.

Section	λ	p_g	**Architecture**	Learning rate	Epochs	Batch size
Section 5.2.1	1	$\mathcal{U}(0.1, 2)$	Bias-free U-Net, 4 down + 4 up blocks	$5e^{-4}$	300	50
Section 5.2.2	1	$\mathcal{U}(0.5, 1.5)$	MLP, input size 100, hidden size 100, depth 5	$1e^{-4}$	300	100
Section 5.3	0.1	$\mathcal{U}(0.1, 2.0)$	Bias-free U-Net, 5 down + 5 up blocks	$5e^{-4}$	100	35
Section 5.4	0.1	$\mathcal{U}(0.2, 1.5)$	Bias-free U-Net, 4 down + 4 up blocks	$5e^{-5}$	400	12

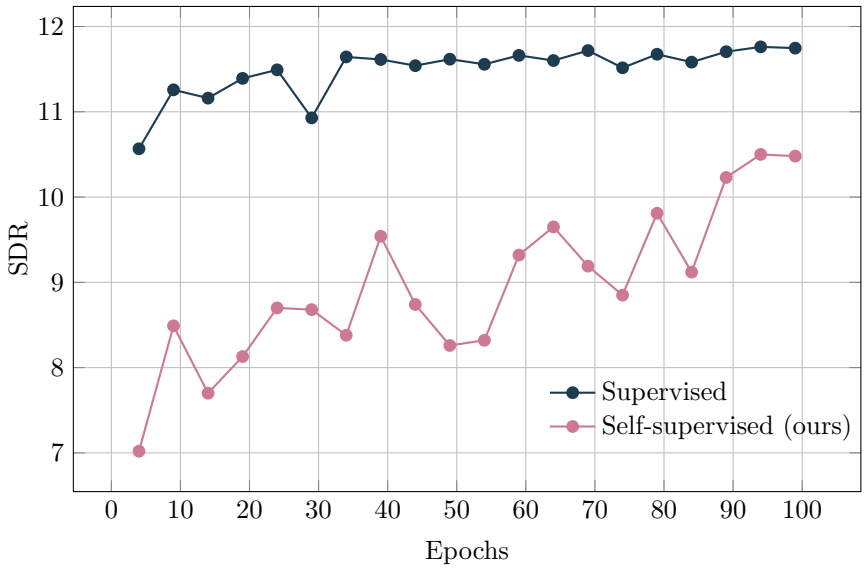

Figure 9: SDR performance on the evaluation dataset during training for supervised and self-supervised methods.